

A Millimeter-Wave Shared-Volume Dual-Aperture Antenna Array with Enhanced Spatial Coverage Efficiency for IoT Devices

Weiguang Song, Grant Gourley, Kun Zhao, Jin Zhang, George Goussetis, *Senior Member, IEEE*, Zhenxiang Yi, *Member, IEEE*, Lei Wang, *Senior Member, IEEE*

Abstract—This paper presents a millimeter-wave shared-volume dual-aperture antenna array with enhanced spatial coverage efficiency for IoT devices. The antenna unit is implemented with two substrate integrated step horns sharing the volume of a cube. The radiation apertures of the two step horns are perpendicular to each other, namely the horizontal aperture and the vertical aperture, enabling a large spatial coverage with a small size. The working bandwidth of the horizontal aperture is from 22 GHz to 37 GHz, and the working bandwidth of the vertical aperture is from 19 GHz to 30 GHz. A 4-element linear array is proposed using the antenna unit. The horizontal and vertical subarrays obtain an average 11.5 dBi and 10.5 dBi realized gain respectively, with -3 dB scanning angle being up to $\pm 35^\circ$ at 27 GHz. A simulation is conducted by deploying the designed array in a smartphone to demonstrate its performance in practical applications. The spatial coverage efficiency of the proposed antenna array is calculated to quantify its spatial coverage capability. A prototype of the 4-element array is fabricated and a good agreement is achieved between the measurement and the simulation.

Index Terms—Antenna array, dual-aperture, millimeter-wave, spatial coverage efficiency, substrate integrated waveguide (SIW).

I. INTRODUCTION

MILLIMETER-WAVE antennas and arrays have been receiving great interests due to the rapid development of wireless communication technology [1]–[3], especially with the widespread promotion and application of the 5th Generation (5G) mobile communication and internet of things (IoT) technology [4]–[6]. As shown in Fig. 1, both wireless communication and IoT technologies play important roles in the construction of smart city, smart industry and smart agriculture. Millimeter-wave has a great advantage over traditional sub-6 GHz band due to its rich spectrum resource,

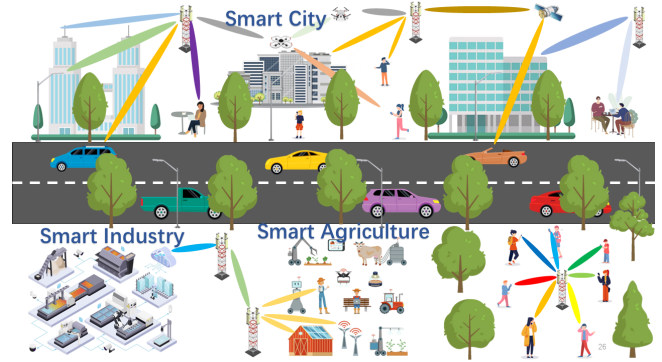


Fig. 1. Millimeter-wave communication systems in the construction of smart cities, smart industries and smart agriculture.

which is very important for application scenarios featured with massive throughput and low latency [7]–[10]. However, the propagating loss of millimeter-wave is much larger than lower frequency waves, causing the signal-to-noise ratio (SNR) of the data received not high enough, thus suppressing the sensitivity and the stability of the entire system [11]–[13]. To overcome this problem, elaborately designed millimeter-wave antennas with high gain are needed to compensate for the propagating loss [14]–[16]. However, a high directivity is typically accompanied by a narrow beamwidth, which limits the spatial coverage efficiency of the antenna. One effective solution is to make millimeter-wave antennas into phased arrays so that those narrow but highly directive beams can be steered flexibly within a certain range determined by the patterns of the antenna units and the structure of the arrays [17]–[20]. In recent years, various millimeter-wave phased antenna arrays with good performance have been proposed, using different array factors or different types of antenna units [21]–[27]. To evaluate the performance of phased arrays in mobile terminals more efficiently and accurately, spatial coverage efficiency is proposed, which reflects the spatial coverage ability of the antenna array by quantified calculation [28]–[30]. This evaluation method is widely applied by many studies to make the simulation or test results of the millimeter-wave antenna arrays closer to their performance in practical application scenarios.

A millimeter-wave shared-volume antenna was conceptually showcased in a conference [31], aiming for large spatial coverage efficiency at limited antenna sizes with simulation

Manuscript Accepted April 2, 2025.

This work has been supported by the EPSRC grant EP/Y003144/2.

(corresponding author: Zhenxiang Yi, Lei Wang)

Weiguang Song is with Southeast University and School of Engineering and Physical Sciences, Heriot-Watt University, Edinburgh, EH14 4AS, United Kingdom (e-mail: ws2032@hw.ac.uk).

Lei Wang is with School of Engineering, Lancaster University, Lancaster, United Kingdom (e-mail: wanglei@ieee.org).

Grant Gourley and George Goussetis are with School of Engineering and Physical Sciences, Institute of Sensors, Signals and Systems, Heriot-Watt University, EH14 4AS Edinburgh, United Kingdom.

Zhenxiang Yi is with the Key Laboratory of MEMS of the Ministry of Education, Southeast University, Nanjing 210096, China (e-mail: xp@seu.edu.cn).

Kun Zhao and Jin Zhang are with Department of Electronic Systems, Aalborg University, Aalborg, Denmark.

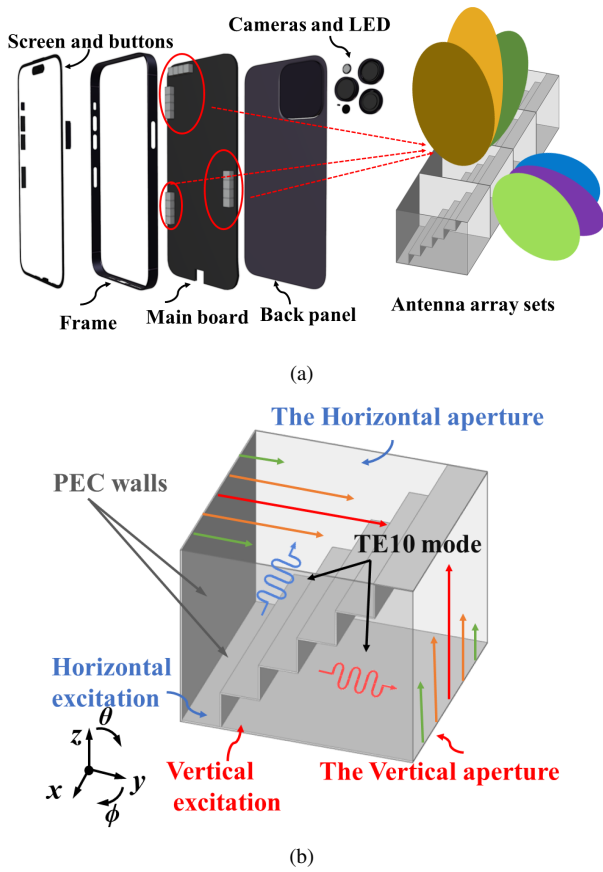


Fig. 2. Concept of the millimeter-wave dual-aperture antenna array in a smart phone. (a) Smart phone with the proposed antenna array, (b) structure of the antenna unit.

proofs. In this paper, the antenna unit is further developed with the instruction of small reflection theory [32] to obtain a better impedance matching for a wider bandwidth. The antenna is implemented using substrate integrated waveguide (SIW) technology, which has great advantages when applied in mobile devices due to its low cost, easy integration and easy fabrication [33]–[36]. A 4-element linear array is designed and deployed in a smartphone to demonstrate the good performance in practical application scenarios. With three designed arrays deployed in a smartphone, the spatial coverage efficiency reaches up to 87.5% at 22.4 dBm EIRP, which is at least 75% higher than any studies referred in this paper. A prototype of the 4-element linear array is fabricated and a good agreement achieved between the simulation and the measurement.

The novel shared-volume dual-aperture antenna structure proposed in this paper increases the spatial coverage efficiency greatly with a very small size, which is of great significance for IoT devices in 5G and even the future 6G millimeter-wave communication, sensing and power transmission system. The proposed tightly coupled step horns with SIW technology enable the implementation of the antenna structure. The feeding method designed for the structure make it easy to fabricate and integrate with radio frequency (RF) circuits. The matching method based on the small reflection theory ensures an outstanding performance of the antenna in terms of energy

efficiency. The matching method also provides an example for antenna design with reflections from multiple impedance discontinuity structures.

This paper is organized as follows. Section II describes the design concept of the antenna unit and array. Section III gives the design procedure of the antenna unit implemented using the SIW technology. Section IV covers the design, analysis and measurement of the 4-element linear array. Finally, conclusions are made in Section V.

II. DESIGN CONCEPT

Antennas in mobile devices working in traditional sub-6 GHz bands are typically in the form of linear metal strips, thus the radiation patterns of these antennas are commonly quasi-omnidirectional. However, antennas in mobile devices working in 5G millimeter-wave bands have to be directional to maximize the communication distance. Thus, phased arrays are needed to make the beams steerable to maximize the spatial coverage. A $1 \times M$ linear antenna array steers the beam along the direction of the array arrangement while the beam in the plane which is perpendicular to the array arrangement is fixed, resulting in a limited spatial coverage. A $N \times M$ antenna array can steer the beam more flexibly around the axis perpendicular to the array structure, obtaining a much larger spatial coverage. However, there is typically no enough space for a smartphone to fit a $N \times M$ antenna array. This study aims to make a compromise between the antenna array size, gain and the spatial coverage using a $1 \times M$ antenna array composed of M compact dual-aperture antenna units, as shown in Fig. 2 (a).

For conventional antenna structures, such as patch and slot antennas, the beam direction is always perpendicular to the aperture on which the electric field is established. Such antennas only have one aperture, therefore, they are only able to cover one direction, which limits the spatial coverage efficiency. The shared-volume dual-aperture structure proposed in this study solves this problem by adding a dimension to the design of the antenna. As shown in Fig. 2 (b), the antenna unit is in the form of a cube. Two adjacent faces of the cube are selected as radiating apertures while the remained four faces are covered with PEC walls. The two radiating apertures are named the horizontal aperture and the vertical aperture, respectively, basing on their position in the Cartesian coordinate system. Several metal stairs split the cube into two step horns to feed the two radiating apertures. By integrating two step horn antennas into one cube, the shared-volume structure make full use of the space occupied by the antenna element, creating two apertures with similar radiating capability but radiating towards different directions, i.e., perpendicular to each other. Each aperture or beam is able to cover areas defined by similar solid angles but the covered areas are not overlapped. Thus, a larger spatial coverage efficiency than conventional antennas can be obtained. When the shared-volume dual-aperture antennas are used to build an antenna array, they can create two subarrays with their two apertures. Each of the subarray is able to steer its beam independently, which obtains even larger spatial coverage efficiency than the antenna elements.

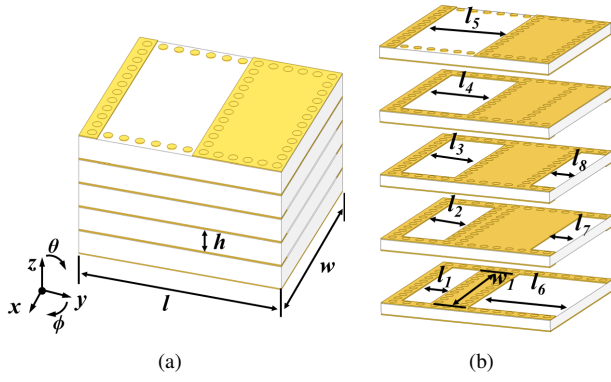


Fig. 3. The antenna unit implemented using SIW technology. (a) The overall geometry. (b) The laminated structure.

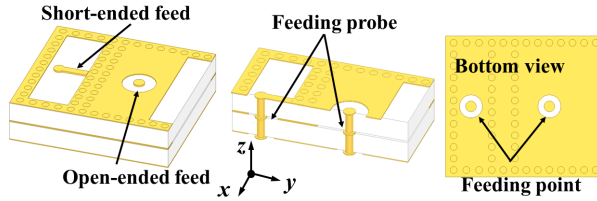


Fig. 4. Feeding design of the antenna unit.

III. ANTENNA UNIT DESIGN

A. Overall Structure

The antenna unit is implemented using multi-layer SIW technique, which is featured with low cost and easy fabrication. The PCB board in use is Rogers RO4003, of which the relative permittivity and dielectric loss tangent are 3.55 and 0.0027, respectively. As shown in Fig. 3, the antenna unit consists of 5 layers of SIW boards with same geometric sizes. To form the step horn which feeds the apertures, part of the copper on the top and bottom side of the SIW boards are etched out for electromagnetic waves to travel through. The edges of the etched area are surrounded with metal vias to prevent the electromagnetic wave from leaking away. For the horizontal aperture, the etched area of the copper increases layer by layer along the z axis direction. Conversely, for the vertical aperture, the etched area of the copper decreases layer by layer along the z axis direction. By stacking all the layers together, the step horns for the horizontal aperture and the vertical aperture are automatically formed.

B. Feeding Design

As shown in Fig. 4, the feeding probes of the two step horns are integrated in the first and second layers. The feeding probes for the two apertures are both inserted into the antenna unit through the holes from the bottom side of the first layer. For the horizontal aperture, to excite the TE_{10} mode in the step horn, one of the strategy is using an open-ended feeding probe to realize the electrical coupling. This requires the probe to be perpendicular to the propagating direction of the TE_{10} mode. To implement such a feeding structure requires a continuous copper plate which can be etched on the xoz -plane wall constructed by the stacked multiple-layer SIW boards.

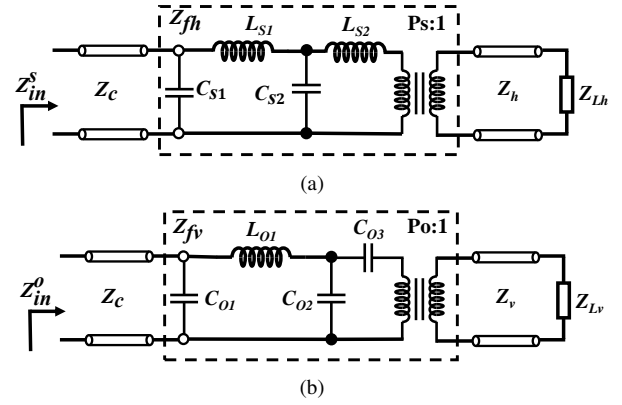


Fig. 5. Equivalent circuits of the feeding structures. (a) Short-ended probe feeding, (b) Open-ended probe feeding.

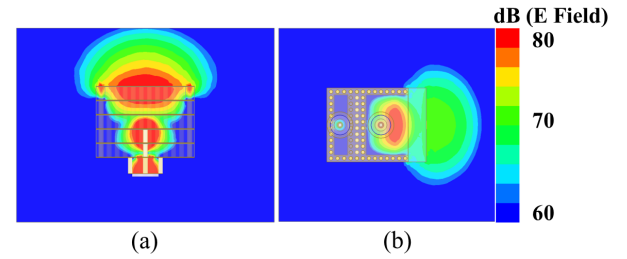


Fig. 6. E field distribution in the antenna unit at 27 GHz. (a) Step horn for the Horizontal aperture, (b) step horn for the vertical aperture.

However, it is challenging for current PCB process to deposit a layer of copper on the side walls of PCB boards. Thus, a short-ended feeding strategy is applied instead, as shown in Fig. 4. For the vertical aperture, the step horn can be excited directly using the open-ended feeding probe. The equivalent circuits of the short-ended and open-ended feeding strategies are given in Fig. 5 (a) and (b), respectively [32], [37]. The impedance induced by the feeding probes are highlighted in the dash line frame and are indicated as Z_{fh} and Z_{fv} . Z_{in}^s and Z_{in}^o represent the input impedance seen from the coaxial cables connected with the feeding probes, of which the characteristic impedance Z_c equals to 50Ω . The radiating impedance of the horizontal aperture and the vertical aperture are indicated as Z_{Lh} and Z_{Lv} , and the impedance of the step horns are indicated as Z_h and Z_v , respectively. As shown in Fig. 6, TE_{10} modes are successfully excited in both the two step horns for the horizontal aperture and the vertical aperture, which demonstrates the feasibility of the feeding design.

C. Impedance Matching Design

Impedance matching design is a widely discussed topic in the design of SIW horn antennas. When the TE_{10} mode excited in the SIW step horn propagates to the aperture, the discontinuity at the interface of the aperture and the free space can cause great reflection, lowering the total efficiency of the antenna significantly. Thus, a proper matching structure is needed. The equivalent circuit of the proposed antenna unit is mapped onto its structure as shown in Fig. 7, where the impedance of the step horns between the feeding probe and the

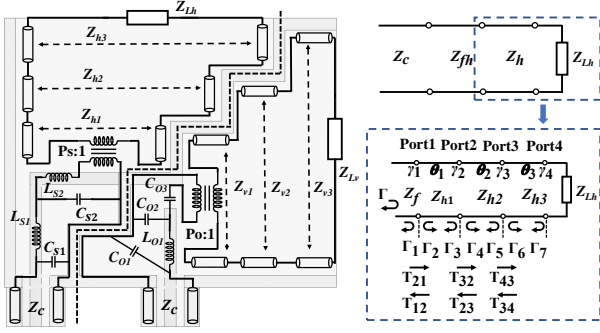


Fig. 7. Equivalent circuit of the antenna and the small reflection theory.

radiating aperture are decomposed into the partial impedance of each corresponding section. Based on the equivalent circuits, the input impedance of the antenna unit can be analyzed using small reflection theory [32].

Taking the analysis of the horizontal aperture as an example, the antenna is divided into four sections shown in Fig. 7. The horizontal aperture antenna consists of four discontinuous impedance segments, i.e. the characteristic impedance of the coaxial cable Z_c , the impedance induced by the short-ended feeding probe Z_{fh} , the impedance of the step horn Z_h , which can be derived from the series of the characteristic impedance of three stages, Z_{h1} , Z_{h2} , Z_{h3} , and finally the impedance of the radiating aperture, Z_{Lh} . Despite the equivalent circuit of the feeding probes simplify the intuitive understanding, no accurate value for Z_{fh} can be obtained for theoretical analysis. Thus, it is essential to study the impedance of the step horn so that the number of variables can be minimized during the impedance matching process. Taking Z_h and Z_{Lh} out of the circuit, the impedance seen by Z_{fh} is indicated by the reflection coefficient Γ . Defining the reflection coefficient seen at port 1 to port 4 as γ_1 to γ_4 , which can be calculated using:

$$\begin{aligned} \gamma_1 &= \Gamma_1 + T_{12}T_{21}\gamma_2e^{-2j\theta_1} + T_{12}T_{21}\gamma_2^2\Gamma_2e^{-4j\theta_1} + \dots \\ &= \Gamma_1 + T_{12}T_{21}\gamma_2e^{-2j\theta_1} \sum_{n=0}^{\infty} \gamma_2^n \Gamma_2^n e^{-2jn\theta_1}, \end{aligned} \quad (1)$$

$$\begin{aligned} \gamma_2 &= \Gamma_3 + T_{23}T_{32}\gamma_3e^{-2j\theta_2} + T_{23}T_{32}\gamma_3^2\Gamma_4e^{-4j\theta_2} + \dots \\ &= \Gamma_3 + T_{12}T_{21}\gamma_3e^{-2j\theta_2} \sum_{n=0}^{\infty} \gamma_3^n \Gamma_4^n e^{-2jn\theta_2}, \end{aligned} \quad (2)$$

$$\begin{aligned} \gamma_3 &= \Gamma_5 + T_{34}T_{43}\gamma_4e^{-2j\theta_3} + T_{34}T_{43}\gamma_4^2\Gamma_6e^{-4j\theta_3} + \dots \\ &= \Gamma_5 + T_{34}T_{43}\gamma_4e^{-2j\theta_3} \sum_{n=0}^{\infty} \gamma_4^n \Gamma_6^n e^{-2jn\theta_3}, \end{aligned} \quad (3)$$

$$\gamma_4 = \Gamma_7, \quad (4)$$

where θ_i represents the phase shift when the wave travels through the waveguide, and the partial reflection coefficients and transmission coefficients are defined as:

$$\Gamma_1 = -\Gamma_2 = \frac{Z_{h1} - Z_f}{Z_{h1} + Z_f}, \quad (5)$$

$$\Gamma_3 = -\Gamma_4 = \frac{Z_{h2} - Z_{h1}}{Z_{h2} + Z_{h1}}, \quad (6)$$

$$\Gamma_5 = -\Gamma_6 = \frac{Z_{h3} - Z_{h2}}{Z_{h3} + Z_{h2}}, \quad (7)$$

$$\Gamma_7 = \frac{Z_{Lh} - Z_{h3}}{Z_{Lh} + Z_{h3}}, \quad (8)$$

$$T_{ij} = 1 + \Gamma_j, \quad (9)$$

$$T_{ji} = 1 + \Gamma_i, \quad (10)$$

where Z_{h1} , Z_{h2} , Z_{h3} are the TE_{10} mode characteristic impedance of the rectangular waveguides, which can be calculated using:

$$Z_{TE_{10}} = \frac{\pi^2 b}{8a} \frac{\eta_0}{\sqrt{1 - \frac{\lambda_0^2}{2a^2 \epsilon_r}}}, \quad (11)$$

where a and b represent the dimension of the rectangular waveguide, $\eta_0 = 377 \Omega$ is the wave impedance of the free space, λ_0 is the wavelength in the free space, and ϵ_r is the relative permittivity of the dielectric filled in the waveguide. While there is no accurate closing equation to calculate Z_{Lh} , it can be obtained by extracting the radiating impedance of an open-ended rectangular waveguide with the same aperture size.

Eventually, with all variables involved in the equations being explained, the desired Γ , which is exactly the γ_1 seen by Z_f can be obtained:

$$\Gamma = \gamma_1. \quad (12)$$

Then, the reflection coefficients of the antenna unit seen from the 50Ω coaxial cable can be obtained by applying the small reflection theory to the network consists of Z_c , Z_{fh} and Γ .

With the analysis above, it can be concluded that the reflection coefficients of the antenna unit is a function of the impedance presented in the equivalent circuit, among which Z_{h3} plays the most significant role, as it is the origin of the calculation. Thus, the impedance matching can be efficiently implemented by adjusting the value of Z_{h3} . Considering (11), Z_{h3} is a function of ϵ_r , and one advantage of the SIW is that it can get the continuously varying ϵ_r simply by removing part of the substrate, which changes the mixed effective relative permittivity of combination between the substrate and the air. This is applied in the impedance matching of the horizontal aperture. As shown in Fig 8 (a), by cutting part of the substrate off the top layer, characteristic impedance of the waveguide changes continuously, which tunes the reflection coefficients of the horizontal aperture. The volume of the cutting part is controlled by l_c . As l_c varies, the reflection coefficients of the horizontal aperture also vary. A wide bandwidth from 22 GHz to 37 GHz is obtained when l_c is between 1.5 mm and 2.0 mm.

According to (11), when designing antennas with different materials, i.e., with different dielectric constant, the characteristic impedance of the rectangular waveguide for different

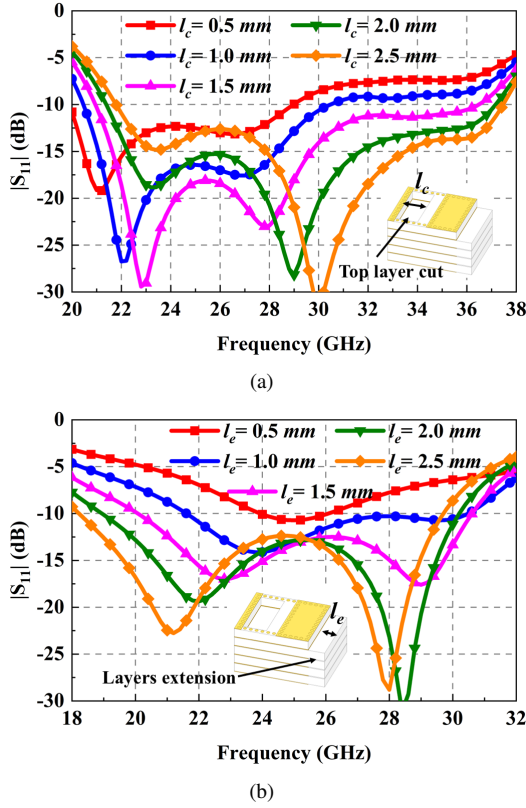


Fig. 8. Matching design of the antenna unit. (a) The horizontal aperture, (b) the vertical aperture.

stages are different. However, the design process will be similar. The target is always to get the minimal reflection coefficients by tuning the characteristic impedance of the final stage rectangular waveguide. For materials with different dielectric constant, the cutting area of the final stage rectangular waveguide will be different for the minimal reflection coefficients. While changing materials also changes the dielectric loss, (11) is not affected, so the calculation of reflection coefficients is not affected. However, the dielectric loss does affect the efficiency of the antenna. The total efficiency of an antenna can be calculated using [38]:

$$e_0 = e_r e_c e_d, \quad (13)$$

where e_0 represents the total efficiency of the antenna, e_r represents the reflection or mismatch efficiency and equals to $1 - |\Gamma|$, and Γ can be calculated using (12), e_c represents the conduction efficiency, e_d represents the dielectric efficiency. The energy efficiency of the antenna is defined as:

$$e_{cd} = \frac{P_{rad}}{P_{in}} = e_c e_d, \quad (14)$$

where e_{cd} represents the energy efficiency, which is also defined as the radiation efficiency, P_{rad} represents the power radiated by the antenna, P_{in} represents the power fed to the antenna element. The energy efficiency does not take the reflection coefficients of the antenna into consideration, it only evaluates the capability of transferring power from RF circuit to the power of free space electromagnetic wave. The higher

TABLE I
PARAMETERS AND TRANSMISSION CHARACTERISTICS OF UNIT CELLS

l_1	l_2	l_3	l_4	l_5	l_6	l_7
1.1 mm	1.6 mm	2.1 mm	2.6 mm	3.1 mm	3.6 mm	1.1 mm
l_8	l_c	l_e	w	w_1	l	h
0.5 mm	1.5 mm	2.0 mm	6.1 mm	5.1 mm	7.0 mm	0.813 mm

the dielectric loss is, the lower the e_{cd} , and the less power is radiated with the same input power. Thus, when designing the antenna with different materials, the priority is to choose a material with low dielectric loss and then tuning the Γ according to the dielectric constant.

The impedance matching of the vertical aperture can be implemented using the same process. However, for the vertical aperture, the cutting method does not perform so well in the impedance matching due to the size limitation caused by the feeding structure. Thus, the dimension of the substrate in (11) is tuned instead by extending it slightly out of the aperture. As shown in Fig 8 (b), the extended volume is controlled by l_e . As l_e increases with a fixed step, the matching performance improves accordingly. A maximal bandwidth from 19 GHz to 30 GHz is obtained when l_e is between 2.0 mm to 2.5 mm. To achieve a balance between the impedance matching and the size of the antenna, l_e is selected between 1.5 mm and 2.0 mm. The final parameters of the antenna unit are given in Table I.

D. Antenna Properties

The normalized radiation patterns of the horizontal aperture and the vertical aperture are plotted in Fig. 9. Within the working bandwidth, the two apertures maintain stable radiation performance with low cross polarization level. As shown in Fig. 10, the comparison between S-parameters of the original and the matched antenna units are made to demonstrate the effect of the matching design. In the figure, $|S_{11}|$ represents the reflection coefficients of the horizontal apertures, $|S_{22}|$ represents the reflection coefficients of the vertical apertures, $|S_{21}|$ represents the mutual coupling between the two apertures. The horizontal aperture and the vertical aperture share the same bandwidth from 24 GHz to 30 GHz with $|S_{11}|$ and $|S_{22}|$ well below -10 dB, which covers the 5G NR bands n257, n258 and n261. The mutual coupling between the two apertures of the matched antenna is below -18 dB. Fig. 11 gives the total efficiency and realized gain of the two apertures. As the structure and size of the two apertures are not exactly the same, the gain of them differs a bit from each other. For the horizontal aperture, the realized gain maintains around 6 dBi in the working band, with the variation less than ± 1 dB. While for the vertical aperture, the realized gain maintains around 5.5 dBi with the variation less than ± 0.5 dB. As both the two apertures are well matched, the total efficiency of the two apertures are both over 90% in the operating bandwidth, and a maximal efficiency up to 96% is obtained, demonstrating their outstanding power transferring capability.

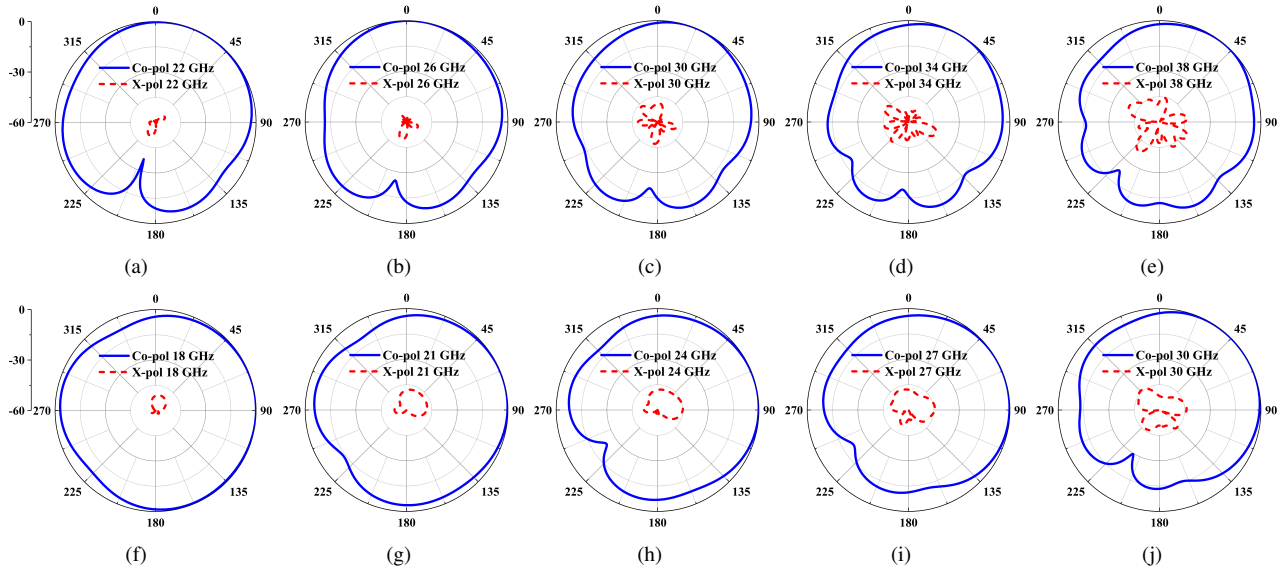


Fig. 9. Normalized radiation patterns of the antenna unit. (a)-(e): Horizontal aperture at 22 GHz, 26 GHz, 30 GHz, 34 GHz and 38 GHz. (f)-(j): Vertical aperture at 18 GHz, 21 GHz, 24 GHz, 27 GHz and 30 GHz.

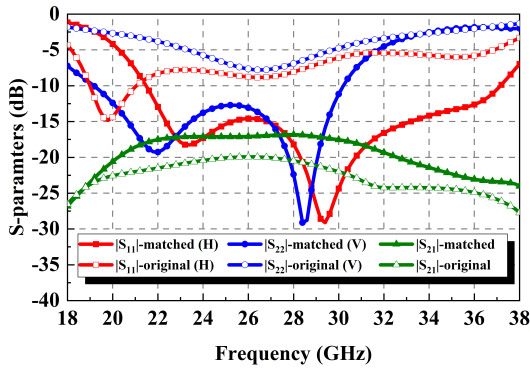


Fig. 10. S-parameters comparison between the original and the matched antenna unit.

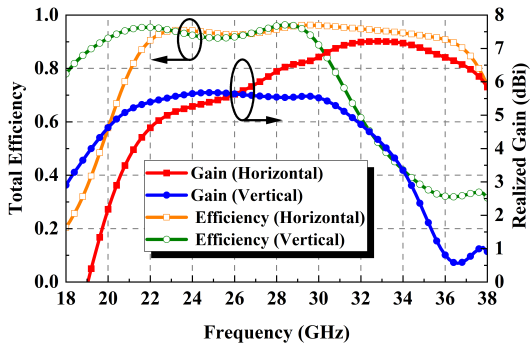


Fig. 11. Simulated total efficiency and realized gain of the antenna unit.

E. Discussion

This section focuses on two main problems, i.e., the feeding and matching of the antenna unit. For the feeding design, the most important task is to excite the proper TE₁₀ mode in the rectangular waveguide. Then, it has to be ensured that the structure for simulation can be fabricated with current PCB

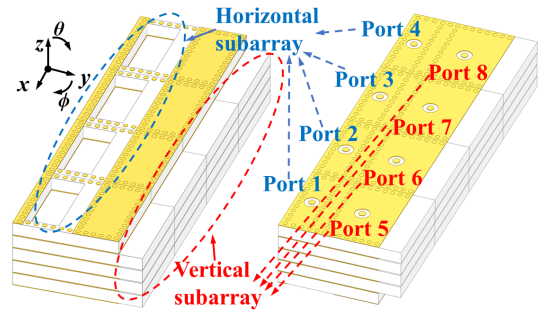


Fig. 12. Geometry of the 4-element shared-volume dual-aperture array.

process. The two conditions above lead the feeding structure to the short-ended probe. For the matching design, the equivalent circuit of the antenna unit is analyzed and the small reflection theory to get the equation for the calculation of the reflection coefficients. By setting the minimal reflection coefficients as the final target, an effective to design the matching structure is found, i.e., tuning the characteristic impedance of the final stage rectangular waveguide. With the feeding and matching problem solved, a final adjustment is made to make sure there is enough clean area for the antenna, which avoids the interference on the performance from adjacent components.

IV. ANTENNA ARRAY ANALYSIS

A. Antenna Array Design

A 4-element linear array is constructed by simply put 4 antenna units next to each other closely. The horizontal apertures of the antenna units make a horizontal subarray while the vertical apertures of the antenna units make a vertical subarray. The horizontal subarray and the vertical subarray together construct the total shared-volume dual-aperture array. As shown in Fig. 12, ports that feed the horizontal subarray are

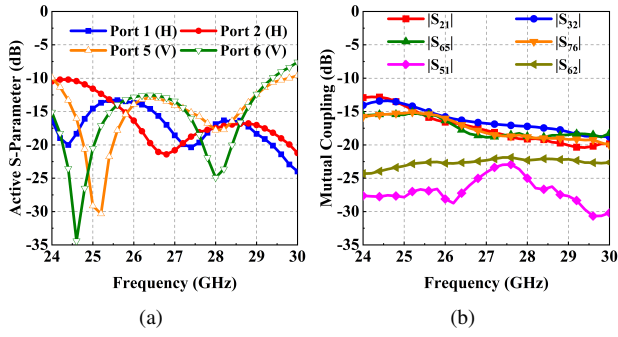


Fig. 13. Active S-parameters and mutual coupling of the 4-element array.

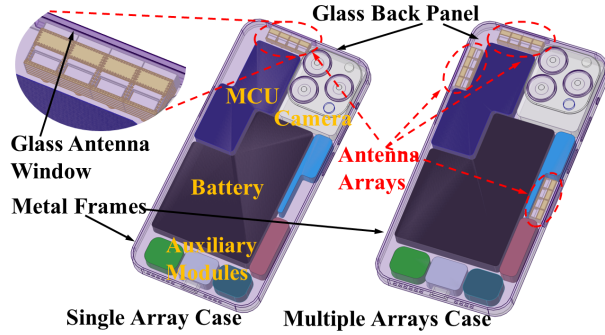


Fig. 14. Array deployment in a smart phone.

marked from 1 to 4 and ports that feed the vertical subarray are marked from 5 to 8.

The active S-parameters of the two subarrays are simulated by exciting 4 ports of one subarray simultaneously while matching the 4 ports of the other subarray to 50 Ω loads. The results are given in Fig. 13 (a). For the horizontal subarray, the active S-parameters of the edge port (Port 1) and the inside port (Port 2) are below -10 dB from 24 GHz to 30 GHz and even higher frequencies. For the vertical subarray, the active S-parameters of the edge port (Port 5) and the inside port (Port 6) are below -10 dB from 24 GHz to 29.5 GHz. As the dual-aperture array is a symmetrical structure, the active S-parameters of the remained four ports are the same as the four ports shown in Fig. 13 (a). The mutual coupling between adjacent apertures are given in Fig. 13 (b). For both the two subarrays, the coupling between the adjacent apertures is below -12 dB. The coupling between the horizontal aperture and the vertical aperture of the same antenna unit in the array is well below -20 dB.

B. Antenna Array Performance with Phone Body Effect

For antenna arrays in mobile devices, the performance is affected by the surrounding physical structures and electronic components. To demonstrate the performance of the designed array in practical application scenarios, it is simulated while being installed in a simplified smart phone model. As shown in Fig. 14, the phone model consists of a metal frame, a glass back panel, a glass front screen and other modules. On the top of the metal frame, an antenna window is designed by replacing the metal part with glass. The antenna array is

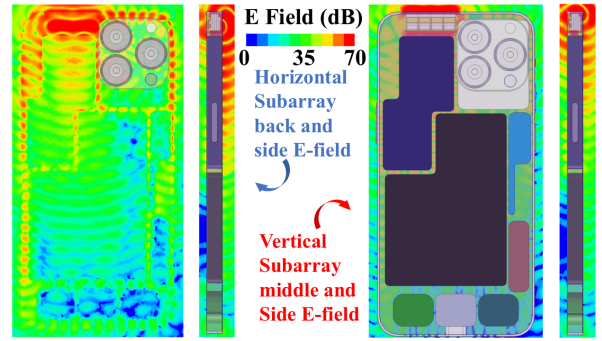


Fig. 15. E field distribution of the arrays when deployed in a smart phone.

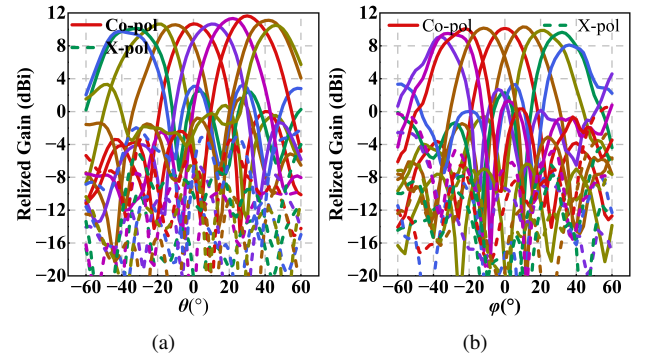


Fig. 16. Radiation patterns of the horizontal subarray and the vertical subarray with phone body effect. (a) Horizontal subarray, (b) Vertical subarray.

installed at the top of the phone model, where the radiation of the horizontal subarray propagates through the glass back panel while the radiation of the vertical subarray propagates through the glass antenna window.

The Electric field distribution of the antenna array is illustrated in Fig. 15. The horizontal subarray contributes to the coverage over the back panel of the phone, while the vertical subarray contributes to the coverage of the space over the head of the phone.

In this design, the back panel and the antenna window are simply flat glasses. However, they can also be specifically designed as lens to customize the radiation pattern of the arrays. The radiation patterns in Fig. 16 demonstrates that the performance of the arrays remains good despite the presence of the phone body. Both the horizontal and the vertical array achieve a scanning range up to $\pm 35^\circ$, with the realized gain being around 11.5 dBi and 10.5 dBi, respectively.

C. Spatial Coverage Efficiency Analysis

Assuming two reflection and polarization-matched antennas aligned for maximum directional radiation and reception in an IoT system, the power received by the IoT device can be calculated using [38]:

$$P_r = P_t G_t G_r \left(\frac{\lambda}{4\pi r} \right)^2, \quad (15)$$

where P_r represents the received power, P_t represents the input power of the transmitter, G_r and G_t represent the

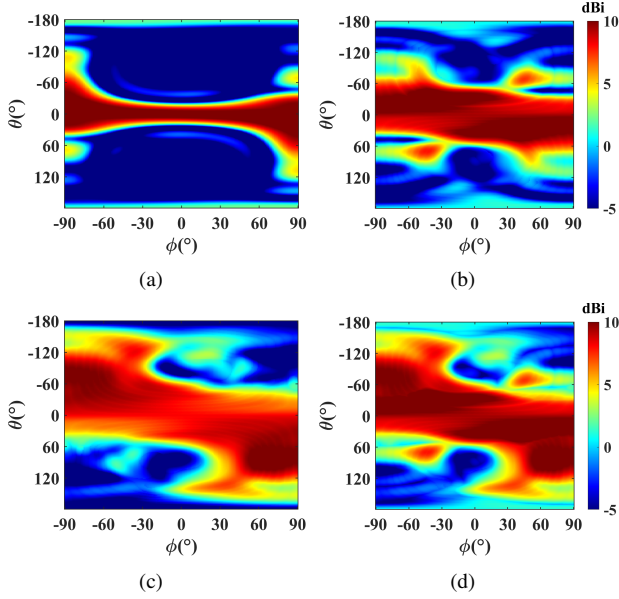


Fig. 17. Realized gain distribution of the 4-element array with phone body effect at 27 GHz. (a) The horizontal radiation pattern with no phase difference, (b) the total scanning radiation pattern of the horizontal subarray, (c) the total scanning radiation pattern of the vertical subarray, (d) the total scanning radiation pattern of the total array.

gain of the receiving antenna and the transmitting antenna, respectively. The remaining terms are defined as the free-space loss factor, where r represents the distance between the two antennas. Due to the high free-space loss, P_r is not likely to exceed the upper power limit of the receiving system. Thus, it is always favorable to increase the dynamic range of the system by increasing p_r . The best approaching to this target is increasing the G_r and G_t and keeping P_t unchanged, as it avoids the potential extra power consumption. The spatial coverage efficiency is the specific term used to evaluate the gain of the antenna in different directions across the spherical space.

The total scanning radiation patterns of the two subarrays are obtained by extracting the maximal achievable realized gain at every angular distribution point from each single scanning radiation pattern, as shown in Fig. 17. The total scanning radiation pattern of the total dual-aperture array is obtained by adding up the total scanning radiation patterns of the two subarrays meanwhile keeping the maximum value of the overlapped part.

To quantify the spatial coverage capability of the total dual-aperture array, the spatial coverage efficiency (η_c) of a certain effective isotropic radiated power (EIRP) with a total input power of 15 dBm is calculated using:

$$\eta_c = \frac{\text{Coverage Solid Angle}}{\text{Maximum Solid Angle}}, \quad (16)$$

where the coverage solid angle is obtained by accumulating the angles where the EIRP is equal to or larger than a set value, and the EIRP can be calculated using:

$$\text{EIRP} = P_t + G_t. \quad (17)$$

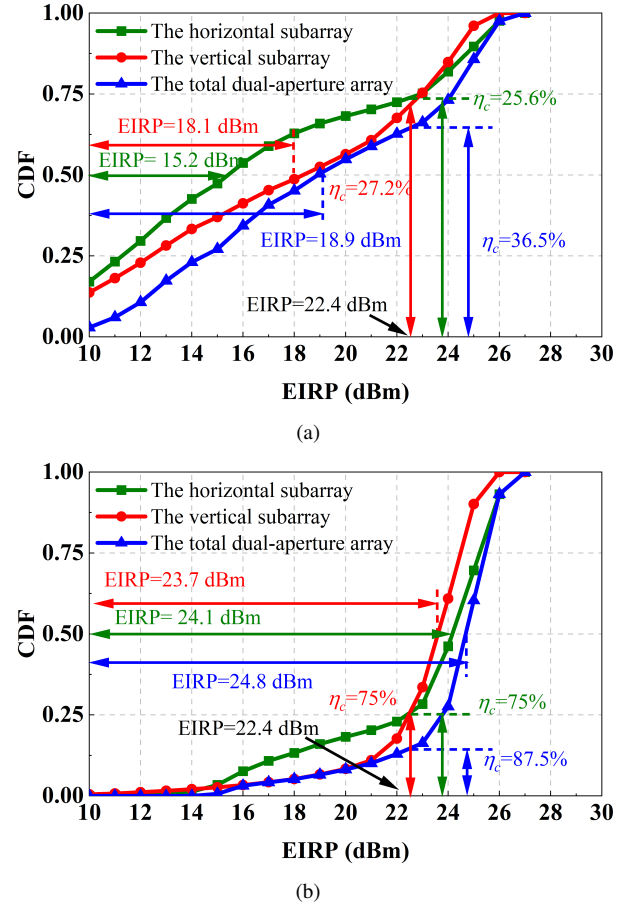


Fig. 18. (a) CDF of single array deployed in one smart phone. (b) CDF of three arrays deployed in one smart phone.

where P_t and G_t represents the total input power and the gain of the antenna array, respectively.

The maximum solid angle is chosen as the surrounding sphere, i.e. 4π steradians [28]. According to the 3GPP R4-2107950, the minimal peak EIRP for handheld user equipment (UE) working at n257, n258 and n261 is 22.4 dBm and the maximal EIRP is 43 dBm. The cumulative distribution function (CDF) concerning the EIRP of the total dual-aperture array can be calculated using:

$$\begin{aligned} \text{CDF}(\text{EIRP}_0) &= \text{P}(\text{EIRP}_{\text{AUT}} \leq \text{EIRP}_0) \\ &= 1 - \eta_c(\text{EIRP}_0), \end{aligned} \quad (18)$$

where $\text{P}(\text{EIRP}_{\text{AUT}} \leq \text{EIRP}_0)$ represents the probability that the measured EIRP from an arbitrary direction of the dual-aperture antenna under test (AUT) takes a value less than or equal to a certain threshold EIRP value EIRP_0 , $\eta_c(\text{EIRP}_0)$ represents the spatial coverage efficiency of the dual-aperture at EIRP_0 [29], [30].

The $\text{CDF}(\text{EIRP}_0)$ of the horizontal subarray, the vertical subarray and the total dual-aperture array are plotted in Fig. 18(a). Taking the EIRP of 22.4 dBm as an example, the η_c of the horizontal subarray and the vertical subarray are 25.6% and 27.2%, respectively. While the η_c of the total dual-aperture array is around 36.5%. For the same η_c of 50%, the EIRP of the horizontal subarray, the vertical subarray and the

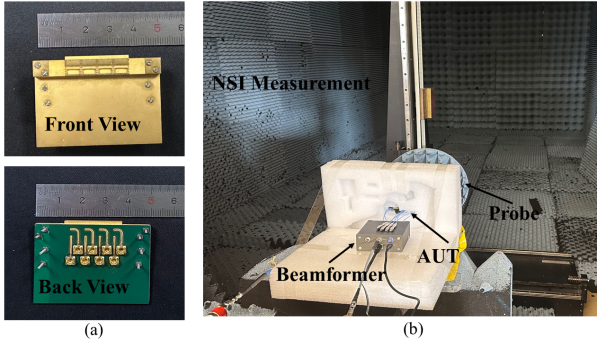


Fig. 19. (a) Antenna array prototype, (b) measurement setup.

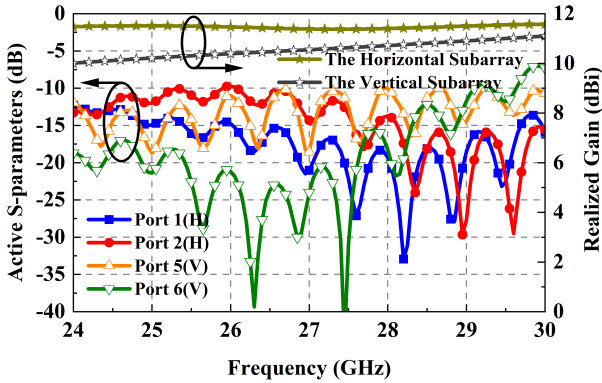


Fig. 20. Measured active S-parameters and realized gain of the fabricated 4-element array.

total dual-aperture array are 15.2 dBm, 18.1 dBm and 18.9 dBm, respectively.

As the structure of the array is very compact, it is feasible to deploy multiple arrays on one smart phone to increase the spatial coverage efficiency, as shown in Fig. 14. The CDF of η_c of three arrays deployed in one smart phone is calculated and plotted in Fig. 18(b). The η_c at 22.4 dBm EIRP in this case is up to 87.5%, with both the horizontal subarray and the vertical subarray being around 75%.

With such high spatial coverage efficiency obtained, the IoT devices equipped with the proposed antenna array is able to maintain high quality communication or high efficiency power transmission in most directions across the free space. As the two apertures of the antenna array work independently, the malfunction of one aperture does not affect the performance of the other aperture, which increases the robustness of the system.

V. PROTOTYPE AND MEASUREMENT

As shown in Fig. 19 (a), a prototype of the antenna array is fabricated using Rogers RO4003 PCB boards. The border of the array is extended for the purpose of stacking and feeding. Although the extended part performs partially as the surrounding metal structures in application scenarios, it does not affect the pattern so much as when it is put inside a smartphone. The active S-parameters of the antenna array is measured using a 4-port vector network analyzer (VNA). When the horizontal subarray is being measured, each port of

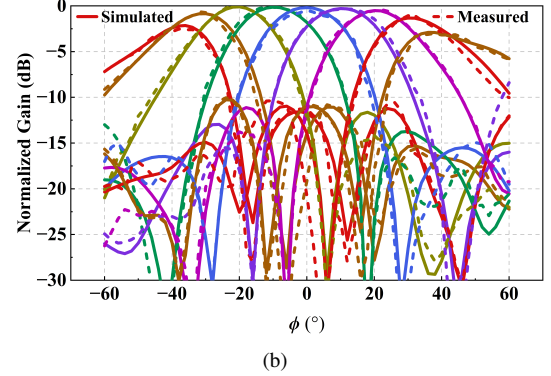
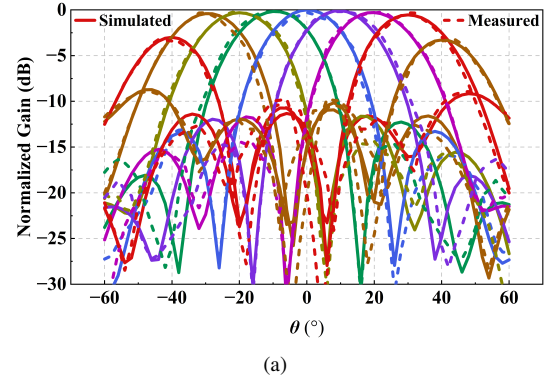


Fig. 21. Measured and simulated normalized Gain of the fabricated 4-element array. (a) Horizontal subarray, (b) vertical subarray.

the vertical array is connected with a 50 Ω broadband load. Then the same operation is conducted to measure the vertical subarray. The beam scanning property of the two subarrays are measured in a chamber using a near-field measurement system with a standard open-ended waveguide working as the probe. The antenna subarray under test is connected to a 4-port beamformer to conduct the beam steering operation, as shown in Fig. 19 (b). The beamformer is capable of feeding each port of one subarray with independent amplitude and phase. The measured active S-parameters of port 1, 2, 5 and 6 are plotted in Fig. 20, where both the horizontal and the vertical subarray obtain a -10 dB bandwidth from 24 GHz to 30 GHz. The measured realized gain of the horizontal subarray maintains around 11.5 dBi with the variation less than ± 0.5 dB, while the measured realized gain of the vertical subarray maintains around 10.5 dBi with the variation less than ± 1 dB. The measured and simulated normalized radiation patterns of the horizontal subarray and the vertical subarray at 27 GHz are compared in Fig. 21 (a) and Fig. 21 (b) respectively. The simulated realized gain in the plot is obtained without the phone body effect. The measurement agrees well with the simulation for both the horizontal subarray and the vertical subarray.

The η_c in terms of EIRP at 22.4 dBm with a total input power of 15 dBm is compared with other previous studies in Table II. For the 1×4 arrays in other studies, the aperture size equal to the product of the width and height of the arrays. However, in this work, the elaborately designed shared-volume dual-aperture antenna unit makes full use of the array size,

TABLE II
COMPARISON OF PERFORMANCES BETWEEN PROPOSED AND RECENT SIW HORN ANTENNAS

Ref.	Frequency (GHz)	Antenna unit type	Array Element	Peak Gain (dBi)	Array Size L×W×H (λ_0^3)	Aperture Size (λ_0^2)	Scanning Angle (Degree)	η_c at 22.4 dBm (%)	Energy Efficiency (%)
[17]	23.4~30	$\pm 45^\circ$ polarized horn	3×4	11.4	1.27×2.49×0.34	2.49×0.34	-30~+30	49	N.A
[22]	25~29	Dual-polarized horn	1×4	8.2	0.32×2.28×0.1	2.28×0.1	-40~+35	0	63-79
[39]	25~31	Stacked patch	1×10	11.7	1×4.8×1.0	4.8×1.0	-65~+65	50	54-75
[40]	27~30.5	Stacked patch	2×3+1×2	13.3	2.3×2.9×0.42	2.3×2.9	-64~+64	40	N.A
[40]	27.5~29	Mesh grid Yagi-Uda and chip antenna	2×4	N.A	1.8×2.6×0.42	1.8×2.6	-70~+70	47.0	N.A
This work	24~30	Shared-volume dual-aperture step horn	3×4	11.5	0.7×2.44×0.45	2.44×0.9	-35~+35	87.5	90-96

obtaining a larger aperture size, which equals to twice the product of the width and height of the array, contributing to the high realized gain and spatial coverage efficiency. The most significant advantage of this feature is that, with the same number of elements, the shared-volume dual-aperture array proposed in this paper obtains a much higher spatial coverage efficiency than any antenna arrays in referred studies. Although some of the studies didn't provide the information of energy efficiency, it is obvious that the 90% to 96% energy efficiency of our study is very high in the absolute value and it is much higher than all provided energy efficiency from other studies, which proves one more advantage of the proposed antenna design method.

With the demonstration by the measurement, the antenna design concept proposed in this study is proved to be effective in resolving the contradiction between high directivity and high spatial coverage efficiency existing in conventional antennas. By increasing one dimension to the antenna design, i.e., integrating two highly-directive and physically perpendicular radiating apertures into a small cube, the spatial coverage efficiency is increased without occupying extra space. Such a highly integrated structure makes the feeding and matching design very challenging. For the feeding design, the short-ended probe feeding is proposed for the horizontal aperture, which makes the antenna easy to be fabricated and integrated with the RF circuit. For the matching design, the small reflection theory is applied to analyze the structure and guide the tuning of the matching structure. Although the antenna design concept proposed in this study is more complex and the designing process is more challenging than conventional antennas, it achieves an outstanding performance in terms of directivity and spatial coverage efficiency. The feeding and matching method proposed in this study also helps increase the design efficiency greatly.

VI. CONCLUSION

This paper proposes a millimeter-wave shared-volume dual-aperture substrate integrated step horn antenna and array with enhanced spatial coverage efficiency. With elaborately

designed impedance matching and feeding structure, both the two apertures of the antenna unit have a working bandwidth over 10 GHz, from 22 GHz to 37 GHz and 19 GHz to 30 GHz, respectively. A 4-element linear array of the unit cell is constructed and simulated when considering the body effect of smartphones. Simulation results demonstrate that the performance of the array remains outstanding with proper designed antenna windows. The working bandwidth of the array covers the 5G NR bands, n257 (26.5 GHz–29.5 GHz), n258 (24.25 GHz–27.5 GHz) and n261 (27.5 GHz–28.35 GHz). With three arrays deployed in one smartphone, the spatial coverage efficiency reaches up to 87.5% at 22.4 dBm EIRP, which is at least 75% higher than any studies referred in this paper. A prototype of the 4-element linear array is fabricated and measured and the measurement agrees well with the simulation. This study provides an effective method to increase spatial coverage efficiency of millimeter-wave antennas. It proves the feasibility of increasing the effective radiating aperture of antennas without increasing the occupied area. It also serves an example of applying small reflection theory in antenna design with multiple reflections. The high spatial coverage efficiency and wide bandwidth obtained with the proposed shared-volume dual-aperture antenna structure in this study increases the signal receiving, remote sensing and power transmission capability of millimeter-wave devices such as unmanned aerial vehicles (UAVs), smartphones and robots in 5G and future 6G millimeter-wave wireless communication and IoT systems. With the robust dual-aperture structure, the antenna can keep working properly even if there is one aperture malfunctions due to block or intensive interference, making it competitive in applications where the environment is complex or anti-jamming function is needed.

REFERENCES

- [1] A. Zanella, N. Bui, A. Castellani, L. Vangelista, and M. Zorzi, "Internet of things for smart cities," *IEEE Internet of Things Journal*, vol. 1, no. 1, pp. 22–32, 2014.
- [2] N. Hussain and N. Kim, "Integrated microwave and MM-wave MIMO antenna module with 360° pattern diversity for 5G internet of things," *IEEE Internet of Things Journal*, vol. 9, no. 24, pp. 24 777–24 789, 2022.

- [3] R. Hussain, "Shared-aperture slot-based sub-6-GHz and MM-wave IoT antenna for 5G applications," *IEEE Internet of Things Journal*, vol. 8, no. 13, pp. 10807–10814, 2021.
- [4] X. Yang, Y. Ji, J. Hu, L. Ge, Y. Li, and K. M. Luk, "Wideband quasi-spherical lens antenna module with 2-D switched beams for 5G millimeter-wave IoT applications," *IEEE Internet of Things Journal*, vol. 11, no. 1, pp. 1217–1227, 2024.
- [5] F. Karami, H. Boutayeb, and L. Talbi, "Directive millimeter-wave end-fire diplexing antenna for IoT applications," *IEEE Internet of Things Journal*, vol. 10, no. 22, pp. 19874–19882, 2023.
- [6] X. Xia, F. Wu, C. Yu, Z. Jiang, J. Xu, S.-Y. Tang, Z. Wang, Y. Yao, and W. Hong, "Millimeter-wave and sub-6-GHz aperture-shared antenna and array for mobile terminals accessing 5G/6G-enabled IoT scenarios," *IEEE Internet of Things Journal*, vol. 11, no. 10, pp. 18808–18823, 2024.
- [7] Y. J. Guo, M. Ansari, R. W. Ziolkowski, and N. J. G. Fonseca, "Quasi-optical multi-beam antenna technologies for B5G and 6G mmwave and thz networks: A review," *IEEE Open Journal of Antennas and Propagation*, vol. 2, pp. 807–830, 2021.
- [8] B. Yang, Z. Yu, J. Lan, R. Zhang, J. Zhou, and W. Hong, "Digital beamforming-based massive MIMO transceiver for 5G millimeter-wave communications," *IEEE Transactions on Microwave Theory and Techniques*, vol. 66, no. 7, pp. 3403–3418, 2018.
- [9] B. Yang, Z. Yu, R. Zhang, J. Zhou, and W. Hong, "Local oscillator phase shifting and harmonic mixing-based high-precision phased array for 5G millimeter-wave communications," *IEEE Transactions on Microwave Theory and Techniques*, vol. 67, no. 7, pp. 3162–3173, 2019.
- [10] W. Kong, Y. Hu, J. Li, L. Zhang, and W. Hong, "2-D orthogonal multibeam antenna arrays for 5G millimeter-wave applications," *IEEE Transactions on Microwave Theory and Techniques*, vol. 70, no. 5, pp. 2815–2824, 2022.
- [11] H. Li, Y. Li, L. Chang, W. Sun, X. Qin, and H. Wang, "A wideband dual-polarized endfire antenna array with overlapped apertures and small clearance for 5G millimeter-wave applications," *IEEE Transactions on Antennas and Propagation*, vol. 69, no. 2, pp. 815–824, 2021.
- [12] K. Wu, Y. J. Cheng, T. Djeraji, and W. Hong, "Substrate-integrated millimeter-wave and terahertz antenna technology," *Proceedings of the IEEE*, vol. 100, no. 7, pp. 2219–2232, 2012.
- [13] S. A. Ali, M. Wajid, A. Kumar, and M. Shah Alam, "Design challenges and possible solutions for 5G SIW mimo and phased array antennas: A review," *IEEE Access*, vol. 10, pp. 88567–88594, 2022.
- [14] C.-X. Mao, M. Khalily, P. Xiao, T. W. C. Brown, and S. Gao, "Planar sub-millimeter-wave array antenna with enhanced gain and reduced side-lobes for 5G broadcast applications," *IEEE Transactions on Antennas and Propagation*, vol. 67, no. 1, pp. 160–168, 2019.
- [15] Y. Al-Alem, S. M. Sifat, Y. M. M. Antar, and A. A. Kishk, "Circularly polarized ka-band high-gain antenna using printed ridge gap waveguide and 3-D-printing technology," *IEEE Transactions on Antennas and Propagation*, vol. 71, no. 9, pp. 7644–7649, 2023.
- [16] W. Zhao, X. Li, Z. Qi, and H. Zhu, "Broadband and high-gain high-order-mode fed open-ended waveguide antenna array for millimeter-wave applications," *IEEE Transactions on Antennas and Propagation*, vol. 70, no. 9, pp. 8614–8619, 2022.
- [17] X. Xia, F. Wu, C. Yu, Z. H. Jiang, R. Lu, Y. Yao, and W. Hong, "Millimeter-wave $\pm 45^\circ$ dual linearly polarized end-fire phased array antenna for 5G/B5G mobile terminals," *IEEE Transactions on Antennas and Propagation*, vol. 70, no. 11, pp. 10391–10404, 2022.
- [18] W. Roh, J.-Y. Seol, J. Park, B. Lee, J. Lee, Y. Kim, J. Cho, K. Cheun, and F. Aryanfar, "Millimeter-wave beamforming as an enabling technology for 5G cellular communications: theoretical feasibility and prototype results," *IEEE Communications Magazine*, vol. 52, no. 2, pp. 106–113, 2014.
- [19] J. Wang, Y. Li, L. Ge, J. Wang, M. Chen, Z. Zhang, and Z. Li, "Wideband dipole array loaded substrate integrated H-plane horn antenna for millimeter waves," *IEEE Transactions on Antennas and Propagation*, vol. 65, no. 10, pp. 5211–5219, 2017.
- [20] Z. Siddiqui, M. Sonkki, K. Rasilainen, J. Chen, M. Berg, M. E. Leinonen, and A. Pärssinen, "Dual-band dual-polarized planar antenna for 5G millimeter-wave antenna-in-package applications," *IEEE Transactions on Antennas and Propagation*, vol. 71, no. 4, pp. 2908–2921, 2023.
- [21] Y. Wang, J. Xu, L. Xiang, K. Chen, and W. Hong, "Low-cost wideband millimeter-wave filtenna and its arrays for miniaturized IoT devices," *IEEE Internet of Things Journal*, vol. 11, no. 16, pp. 27073–27084, 2024.
- [22] J. Zhang, K. Zhao, L. Wang, G. F. Pedersen, and S. Zhang, "Wideband low-profile dual-polarized phased array with endfire radiation patterns for 5G mobile applications," *IEEE Transactions on Vehicular Technology*, vol. 70, no. 9, pp. 8431–8440, 2021.
- [23] J. Zhang, K. Zhao, L. Wang, S. Zhang, and G. F. Pedersen, "Dual-polarized phased array with end-fire radiation for 5G handset applications," *IEEE Transactions on Antennas and Propagation*, vol. 68, no. 4, pp. 3277–3282, 2020.
- [24] L. Wang and Q. Liao, "Wideband multibeam SIW horn array with high beam isolation and full azimuth coverage," *IEEE Transactions on Antennas and Propagation*, vol. 69, no. 9, pp. 6070–6075, 2021.
- [25] J. Seo, I. Yoon, J. Jung, J. Ryoo, J. Park, W. Lee, D. Ko, and J. Oh, "Miniaturized dual-band broadside/endfire antenna-in-package for 5G smartphone," *IEEE Transactions on Antennas and Propagation*, vol. 69, no. 12, pp. 8100–8114, 2021.
- [26] Y. Wang and F. Xu, "Shared aperture 4G LTE and 5G mm-wave antenna in mobile phones with enhanced MM-wave radiation in the display direction," *IEEE Transactions on Antennas and Propagation*, vol. 71, no. 6, pp. 4772–4782, 2023.
- [27] J. Wang, Y. Cao, W. Che, and Q. Xue, "Millimeter-wave beam-scanning phased array with switchable broadside and endfire radiation pattern using phase-controlled elements," *IEEE Transactions on Antennas and Propagation*, vol. 72, no. 3, pp. 2347–2354, 2024.
- [28] J. Helander, K. Zhao, Z. Ying, and D. Sjöberg, "Performance analysis of millimeter-wave phased array antennas in cellular handsets," *IEEE Antennas and Wireless Propagation Letters*, vol. 15, pp. 504–507, 2016.
- [29] B. Xu, Z. Ying, L. Scialacqua, A. Scannavini, L. J. Foged, T. Bolin, K. Zhao, S. He, and M. Gustafsson, "Radiation performance analysis of 28 GHz antennas integrated in 5G mobile terminal housing," *IEEE Access*, vol. 6, pp. 48088–48101, 2018.
- [30] K. Zhao, S. Zhang, Z. Ho, O. Zander, T. Bolin, Z. Ying, and G. F. Pedersen, "Spherical coverage characterization of 5G millimeter wave user equipment with 3GPP specifications," *IEEE Access*, vol. 7, pp. 4442–4452, 2019.
- [31] W. Song, Z. Yi, J. Zhang, K. Zhao, and L. Wang, "Shared-volume millimeter-wave substrate integrated step horn antennas and arrays," in *2023 17th European Conference on Antennas and Propagation (EuCAP)*, 2023, pp. 1–4.
- [32] D. M. Pozar, *Microwave engineering /*, 4th ed. New Delhi :: Wiley,, c2012.
- [33] L. Wang, M. Esquius-Morote, H. Qi, X. Yin, and J. R. Mosig, "Phase corrected H-plane horn antenna in gap SIW technology," *IEEE Transactions on Antennas and Propagation*, vol. 65, no. 1, pp. 347–353, 2017.
- [34] W. Song, Z. Yi, and L. Wang, "Millimeter-wave substrate-integrated corrugation-loaded H-plane horn antenna with beamwidth and back radiation suppression," *IEEE Antennas and Wireless Propagation Letters*, vol. 22, no. 10, pp. 2402–2406, 2023.
- [35] C. Segura-Gómez, A. Palomares-Caballero, A. Alex-Amor, J. Valenzuela-Valdés, and P. Padilla, "Modular design for a stacked SIW antenna array at Ka-band," *IEEE Access*, vol. 8, pp. 158568–158578, 2020.
- [36] M. Kuznetsov and S. K. Podilchak, "Printed SIW horn and aperture design for surface-wave control and power routing by genetic algorithm optimization," in *2021 IEEE International Symposium on Antennas and Propagation and USNC-URSI Radio Science Meeting (APS/URSI)*, 2021, pp. 1651–1652.
- [37] S. Saad, "A more accurate analysis and design of coaxial-to-rectangular waveguide end launcher," *IEEE Transactions on Microwave Theory and Techniques*, vol. 38, no. 2, pp. 129–134, 1990.
- [38] C. A. Balanis, *Antenna theory: analysis and design*. John Wiley & sons, 2016.
- [39] C. Deng, D. Liu, B. Yektakhah, and K. Sarabandi, "Series-fed beam-steerable millimeter-wave antenna design with wide spatial coverage for 5G mobile terminals," *IEEE Transactions on Antennas and Propagation*, vol. 68, no. 5, pp. 3366–3376, 2020.
- [40] H. Kim and S. Nam, "Performance enhancement of 5G millimeter wave antenna module integrated tablet device," *IEEE Transactions on Antennas and Propagation*, vol. 69, no. 7, pp. 3800–3810, 2021.



Weiguang Song received the B.S. degree in Vehicle Engineering from Jiangsu University of Technology, Changzhou, China, in 2020. He received the M.S. degree in Electronics and Information from Southeast University, Nanjing, China, in 2023. He is currently pursuing the joint Ph.D. degree at the University of Edinburgh and Heriot-Watt University, Edinburgh, UK. His research focuses on active integrated antenna and arrays for millimeter-wave communication systems and power amplifiers for integrated active antenna arrays for satellite commu-

nications.

Grant Gourley (Member, IEEE) received the M.Eng. degree in electrical and electronic engineering in 2020 and is currently pursuing the Ph.D. degree at Heriot-Watt University, Edinburgh, U.K. His research focuses on reconfigurable antennas and metasurfaces based on vanadium dioxide (VO_2), as well as millimeter-wave devices for advanced communication and sensing applications.



Kun Zhao received the B.S. degree in Communication Engineering from Beijing University of Posts and Telecommunications (BUPT), Beijing, China in 2010, M.S. and Ph.D. degree from Royal Institute of Technology (KTH), Stockholm, Sweden, in 2012, and 2017, respectively.

Currently, he is a researcher of antenna technology and a 3GPP RAN4 delegate in Sony R&D Center Lund, Sweden. He has been an industrial postdoc in Antennas, Propagation and Radio Networking, Aalborg University, Denmark. He has also been a

visiting researcher at the Department of Electrical and Information Technology, Lund University, Sweden. His current research interests include mm-wave and cm-wave antennas and propagation, MIMO antenna systems, user body interactions and body centric wireless communications.



Jin Zhang received the B.E. degree from the University of Electronic Science and Technology of China, Chengdu, China, in 2012 and the Ph.D. degree in millimeter-wave antennas for 5G mobile terminals and base stations from Aalborg University, Aalborg, Denmark, in 2020. During the study of the Ph.D, she was a visiting researcher at Aalto University, Espoo, Finland. She was a research assistant and postdoctoral researcher in Aalborg University from 2020 to 2022. Her research interests include mm-wave, dual-polarized, shared aperture antennas and

arrays.

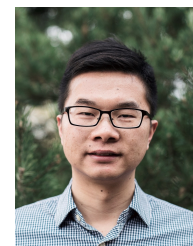


George Goussetis (S 99, M 02, SM 12) received the Diploma degree in Electrical and Computer Engineering from the National Technical University of Athens, Greece, in 1998, and the Ph.D. degree from the University of Westminster, London, UK, in 2002. In 2002 he also graduated B.Sc. in physics (first class) from University College London (UCL), UK. In 1998, he joined Space Engineering (now Airbus DS) in Italy, as RF Engineer and in 1999 the University of Westminster, UK, as a Research Assistant. Between 2002 and 2006 he was a Senior

Research Fellow at Loughborough University, UK. He was Assistant Professor with Heriot-Watt University, Edinburgh, UK between 2006 and 2009 and Associate Professor with Queen's University Belfast, UK, between 2009 and 2013. In 2013 he joined Heriot-Watt and was promoted to Professor in 2014. He is currently the Associate Executive Dean for Enterprise at Heriot-Watt University. He has authored or co-authored over 500 peer-reviewed papers several book chapters one book and six patents. His research interests are in the area of microwave and antenna components and subsystems with particular focus on their applications in satellite systems. Dr. Goussetis held research fellowships from the Onassis foundation in 2001, the UK Royal Academy of Engineering between 2006-2011, and European Commission Marie-Curie in 2011-12 and again in 2014-17. He is the recipient of several awards including the 2011 European Space Agency young engineer of the year prize, the 2016 Bell Labs prize and the best IEEE Proceedings paper 2024. Dr. Goussetis served as Associate Editor to the IEEE Antennas and Wireless Propagation Letters between 2014-18 and as Chair of the European Conference of Antennas and Propagation (EuCAP) 2024.



Zhenxiang Yi (M'15) received the B.S. and Ph.D. degrees from Southeast University, Nanjing, China, in 2009 and 2015, respectively. He is currently a full Professor with the Key Laboratory of MEMS, Ministry of Education, Southeast University. His research is mainly focused on wind/flow sensors, antennas and biosensors. He has published over 80 journal papers and held 25 patents.



Lei Wang (Senior Member, IEEE) received the Ph.D. degree in electromagnetic field and microwave technology from the Southeast University, Nanjing, China in 2015. From 2014 to 2016, he was a Research Fellow in the Swiss Federal Institute of Technology (EPFL) in Lausanne, Switzerland. From 2016 to 2017, he was a Postdoc in the KTH Royal Institute of Technology in Stockholm, Sweden. From 2017 to 2020, he was an Alexander von Humboldt fellow in the Hamburg University of Technology in Hamburg, Germany. From 2020 to 2023, he was

an Assistant Professor in the Heriot-Watt University in Edinburgh, United Kingdom. Since 2024, he is an Associate Professor (Senior Lecturer) in the Lancaster University in Lancaster, United Kingdom. His research includes antenna theory and applications, active electronically scanning arrays, integrated antennas and arrays, substrate-integrated waveguide antennas, leaky-wave antennas, wireless power transfer, and wireless propagations.

He has published more than 100 peer-review papers, book chapters, in addition to UK&US patents. He is the awardee of the National PhD Scholarship in China (2014), the Swiss Government Excellence Scholarship (2014), the Alexander von Humboldt fellowship (2016), Principal Investigator grant from German Research Foundation (DFG) (2020), the British Royal Society research grant (2022), the UK EPSRC international collaboration grant (2023), the Innovate UK grants (2024, 2025) and the Sony Research Award (2025). Moreover, he received the Best Poster Award in iWAT (2018), the Best Paper Award in UCET (2020), and the Best Antenna Paper Award in EuCAP (2023). He also supervised students winning the Honourable Mentioned Best Student Paper Award in APS (2021), the Best Student Paper Award in UCMMT (2022), and the Second Place Winner in IWS (2023).